# Prediction Method and Analysis of Thermal Field in Nanocrystalline Core High-Frequency Transformer Considering Leakage Flux Induced Power Loss

Zhanlei Liu, *Student Member, IEEE*, Lingyu Zhu, *Senior Member, IEEE*, Guanhua Zhang, Yongliang Dang, Shitong Zhang, Shengchang Ji, *Member, IEEE*, and Nan Liu

***Abstract*—Accurate thermal field prediction is the cornerstone of thermal design of high-frequency transformer (HFT). The leakage flux induced power loss (LFPL), which includes leakage flux eddy current loss (LFECL) and leakage flux core loss (LFCL), can increase the hotspot temperature of nanocrystalline core HFT. This article proposes a coupled thermal field prediction method for nanocrystalline core HFT considering LFPL and analyzes the thermal field characteristics. First, the LFPL density distributions in nanocrystalline core are analyzed with finite element method, demonstrating high LFPL density on surface ribbons. Then, a coupled thermal field prediction method for nanocrystalline core HFT considering LFPL is proposed. The total thermal field is calculated by summation of thermal fields with LFECL, LFCL, and main flux core loss and winding loss. The thermal fields with LFPL are calculated with unidirectional magnetic-thermal coupled method, in which LFPL densities are calculated by proposed equivalent frequency domain simulation method and coupled to heat transfer module. The temperature dependences of power losses are considered for high-accuracy thermal field prediction. With the proposed method, the temperature calculation errors are reduced to below 3 °C. Finally, the thermal field characteristics are analyzed. Finite element simulation results show that hotspot temperatures will be greatly increased by LFPL. The proposed method can help improve the thermal design of nanocrystalline core HFT.**

***Index Terms*—High-frequency transformer (HFT), leakage flux induced power loss (LFPL), nanocrystalline core, thermal field prediction.**

## I. Introduction

THE rapid development of renewable energy [1], [2], [3], data center [1], [4], railway transportation [1], and energy storage station [1], [5] has promoted the application of the solid-state transformer (SST). High-frequency transformer (HFT) [6], [7], [8] is an important component in SST. Due to high power loss density and low heat transfer efficiency, the hotspot temperature of HFT is usually high. The overheating of HFT can lead to insulation degradation and device failure. Hence, accurate prediction of the thermal field in HFT is the cornerstone of thermal design to avoid overheating and enable reliable operation.

The thermal field prediction methods of HFT mainly include lumped parameter thermal model (LPTM) [9], [10], [11], [12], [13], [14] and finite element model (FEM) [15], [16], [17], [18], [19], [20], [21]. The LPTM can be adopted for temperature estimation with low computation cost. In [9], [10], and [11], the LPTM is used for fast thermal modeling of HFT in the design stage. In [12] and [13], analytical models for thermal resistance of solid wire or litz wire are proposed to improve winding temperature estimation accuracy. In [14], three-dimensional geometry and frequency-dependent effect are considered for accurate thermal field prediction of planar HFT. Despite the low computation cost, LPTM cannot accurately predict the temperature distribution or hotspot temperature in HFT. The FEM can be applied for high-accuracy thermal field prediction. In [15] and [16], homogenization FEM is used for accurate thermal modeling of windings in electric machines and magnetic components. In [17], [18], and [19], FEM and computational fluid dynamics simulation are implemented to predict the thermal field of HFT. In [20], a multiphysics coupled model considering electrothermal interactions is developed for precise thermal field prediction. In [21], a multilevel boundary-coupled method coupling 2-D and 3-D FEMs with consideration of temperature-dependent power losses is proposed for efficient thermal field prediction.

The thermal field of HFT is determined by power loss as well as its distribution characteristics. A local high power loss density can significantly increase the local hotspot temperature. Despite the improved thermal field prediction accuracy with LPTM or FEM, the power loss distribution characteristics are not fully considered in [9], [10], [11], [12], [13], [14], [15], [16], [17], [18], [19], [20], and [21]. For a gapped nanocrystalline core, the fringing flux around the air gap can introduce additional gap loss [22], which is mainly concentrated around the air gap and contributes to a temperature rise around it. In [23] and [24], LPTMs are proposed to deal with the nonuniform loss distribution issue and predict the hotspot temperature around the

Received 18 September 2025; revised 28 October 2025; accepted 19 December 2025. Date of publication 24 December 2025; date of current version 20 March 2026. Recommended for publication by Associate Editor W. Martinez. *(Corresponding author: Lingyu Zhu.)*

Zhanlei Liu, Lingyu Zhu, Guanhua Zhang, Yongliang Dang, Shitong Zhang, and Shengchang Ji are with the State key Laboratory of Electrical Insulation and Power Equipment, Xi'an Jiaotong University, Xi'an 710049, China (e-mail: lzl0283@stu.xjtu.edu.cn; zhuly1026@xjtu.edu.cn; zgh15020253083@stu.xjtu.edu.cn; dyl877759724@stu.xjtu.edu.cn; ZSTong@stu.xjtu.edu.cn; jsc@xjtu.edu.cn).

Nan Liu is with State Grid Shaanxi Comprehensive Energy Services Company, Ltd., Xi'an 710100, China (e-mail: liunan@zhny.sn.sgcc.com.cn).

Color versions of one or more figures in this article are available at https://doi.org/10.1109/TPEL.2025.3647718.

Digital Object Identifier 10.1109/TPEL.2025.3647718

air gap for the gapped nanocrystalline core inductor. However, the LPTM cannot precisely estimate the hotspot temperature around the air gap. Thermal FEM results are also presented in [23] to demonstrate the precise temperature distribution in the core.

Leakage flux induced power loss (LFPL) [25], [26], [27], which is defined as the summation of leakage flux core loss (LFCL) and leakage flux eddy current loss (LFECL), is significant for medium-voltage high-power nanocrystalline core HFT. The LFECL comes from the eddy current in surface ribbons of nanocrystalline core induced by normal leakage flux and the LFCL comes from the high flux density in surface ribbons of the core caused by concentration of leakage efflux density. In [25], the LFECL resistance measurement and calculation methods are proposed. In [26], the practical nonuniform flux density distribution calculation method is introduced and the nonuniform flux density distribution characteristics are analyzed. In [27], the LFPL mechanism is analyzed and a high-accuracy LFPL calculation method considering surface ribbons saturation is proposed for the first time. It proves that the LFPL is non-negligible compared with main flux induced core loss, especially for high-voltage, high-power, and magnetic-integrated nanocrystalline core HFT. In addition to its large value, the distribution of LFPL is very nonuniform. The LFPL is concentrated in surface ribbons of nanocrystalline core, resulting in local high LFPL densities and increased temperature. However, the impact of LFPL on HFT temperature rise is unclear yet. The LFPL is usually overlooked in thermal field prediction of nanocrystalline core HFT, resulting in an underestimation of hotspot temperature.

The high-accuracy thermal field prediction of HFT caused by LFPL faces three main challenges. First, the LFPL distribution is very nonuniform and shows strong dependences on HFT dimensions and structures. Therefore, it is difficult to characterize the nonuniform structure-dependent loss distribution and predict the thermal field accurately by LPTM. Second, since the excitation voltage and current waveforms are nonsinusoidal, predicting the thermal field caused by LFPL by the summation of thermal fields under all harmonic excitations is very time-consuming. Third, the concentration of leakage flux in surface ribbons of nanocrystalline core may result in surface ribbons saturation. The surface ribbons saturation will change the electromagnetic field distribution as well as the LFPL. It is difficult to take the surface ribbons saturation effect into account in either LPTM or thermal FE simulation.

To address the aforementioned challenges, this article proposes an improved magnetic-thermal coupled method for high-accuracy thermal field prediction of nanocrystalline core HFT and carries out thermal field characteristics analysis. The main contributions of this article are as follows.

1) The LFECL density and LFCL density distributions in nanocrystalline core of HFT are calculated with the FE method. Simulation results show the concentration of LFPL and high LFPL density in surface ribbons.
2) An improved magnetic-thermal coupled method for thermal field prediction of nanocrystalline core HFT considering LFPL is proposed. The total thermal field is calculated by the summation of thermal fields caused by LFECL, LFCL, main flux core loss, and winding loss. A fundamental-frequency sinusoidal current is proposed to equivalently calculate the LFECL density under nonsinusoidal current considering surface ribbons saturation. An analytical equation and an attenuation factor are used to calculate the LFCL density. In the proposed method, the LFECL density and LFCL density are calculated by a single frequency-domain FE simulation each and then coupled to the heat transfer module to calculate the thermal field. The temperature dependences of power losses are considered for high-accuracy thermal field prediction. Compared with the traditional approach without considering LFPL, the proposed method reduces the thermal field prediction errors from over 20 °C to below 3 °C.
3) The thermal field characteristics of nanocrystalline core HFT are analyzed. Simulation results show that the temperature hotspot is located in surface ribbons of the core, which is surrounded by the windings. The high LFPL density in surface ribbons can increase the HFT hotspot temperature by more than 20 °C. Therefore, the LFPL should be taken into considerations for high-accuracy thermal field prediction. Enhanced cooling strategies, such as using high-thermal-conductivity insulation materials or embedding heat pipes or water cooling plate may be necessary for efficient cooling of temperature hotspot.

The rest of this article is organized as follows. In Section II, the LFECL density and LFCL density distributions in nanocrystalline core are analyzed by FEM. In Section III, the principles of the proposed thermal field prediction method and other comparison methods are introduced. In Section IV, two nanocrystalline core HFT prototypes are made. Experimental validations of the proposed thermal field prediction method are provided. Thermal field characteristics of the two nanocrystalline core HFT prototypes are analyzed. Section V concludes this article.

## II. Analysis of Core Loss Density Distribution

Since the nanocrystalline core is made by rolling of ribbons, the permeability and conductivity of nanocrystalline core are anisotropic, resulting in a concentration of leakage flux in surface ribbons and introducing significant LFCL and LFECL [25], [26]. The LFCL and LFECL are non-negligible compared with the main flux induced core loss. In addition, the LFCL and LFECL are concentrated in surface ribbons of the core with a small volume. Therefore, the LFCL density and LFECL density in core surface can be high, resulting in local temperature hotspots in the core surface area.

In this article, FE models for two nanocrystalline core HFT prototypes are established to calculate the LFCL density and LFECL density and compare them with main flux induced core loss density in the core. The nanocrystalline cores used in this article are made by Fe-based nanocrystalline alloy ribbons from Changzhou Chuangming Magnetic Material Technology Co., Ltd in China. The specific composition of the alloy is $Fe_{73.5}Cu_1Nb_3Si_{15.5}B_7$. The first HFT prototype is made with a cut rectangular core and separated windings. The windings are made with litz wire (1000 strands and AWG38). The number of layers of primary and secondary windings are both two. The turn

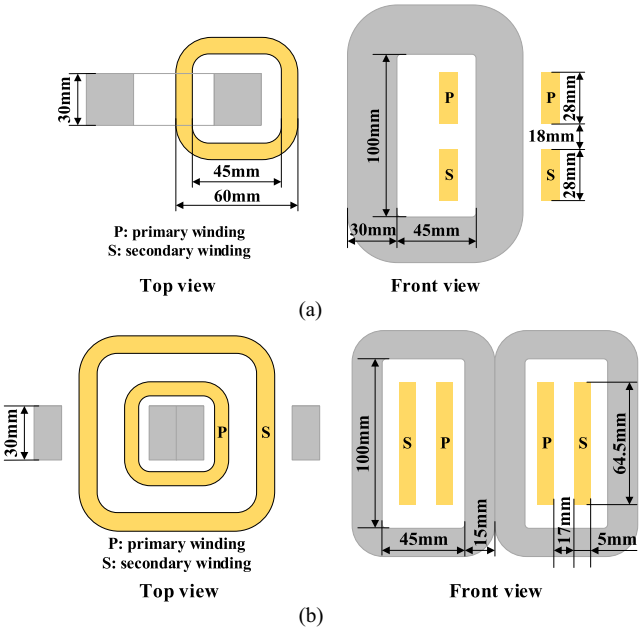


Fig. 1. Structures and sizes of (a) HFT prototype with rectangular core and separated windings and (b) HFT prototype with dual-rectangular (EE) core and concentric windings.

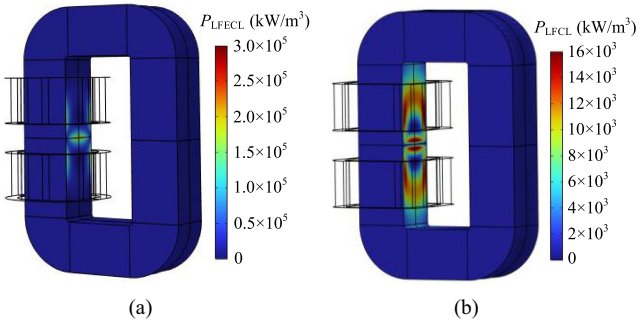


Fig. 2. (a) LFECL density distribution in the core under fundamental frequency current excitation without considering surface ribbons saturation. (b) LFCL density distribution in the core without considering surface ribbons saturation for the first HFT prototype.

ratio is 11:11. The leakage inductance at a 20 kHz sinusoidal signal is 26.4 $\mu$H. The second HFT prototype is made with cut dual-rectangular (EE) core and concentric windings. The windings are made with litz wire (1000 strands and AWG38). The number of layers of primary and secondary windings are both one. The turn ratio is 14:14. The leakage inductance at 20 kHz sinusoidal signal is 16.6 $\mu$H. The structures and sizes of these two HFT prototypes are shown in Fig. 1.

Taking the DAB converter with single-phase-shift (SPS) modulation as an example of load condition, when the first HFT prototype works under primary and secondary voltages of 200 V and a phase shift angle of 25°, the main flux density amplitude $B_m$ in the core is 0.32 T and the winding current amplitude is 25.8 A. The LFECL density distribution in the core under fundamental-frequency current excitation without considering surface ribbons saturation is shown in Fig. 2(a). The LFCL density distribution in the core without considering surface ribbons saturation is shown in Fig. 2(b). While the main flux

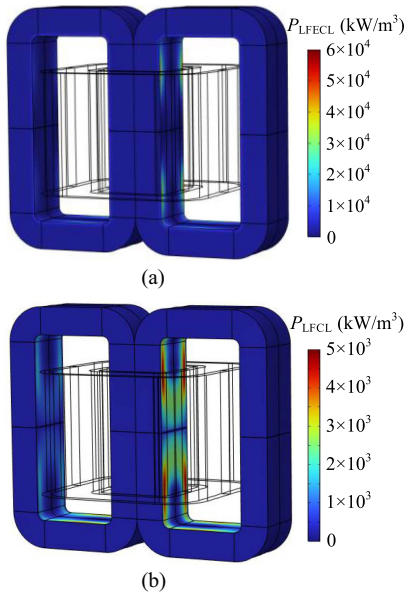


Fig. 3. (a) LFECL density distribution in the core under fundamental frequency current excitation without considering surface ribbons saturation. (b) LFCL density distribution in the core for the second HFT prototype.

induced core loss density is about 23 kW/m$^3$ under $B_m = 0.32$ T, the maximum LFECL density and maximum LFCL density in core surface areas are about 13 000 and 700 times of the main flux induced core loss density respectively. Despite the very high LFECL density and LFCL density, the LFECL, LFCL, and main flux induced core loss are 11.1, 1.8, and 7.9 W, respectively.

When the second HFT prototype works under primary and secondary voltages of 200 V and phase shift angle of 25°, the main flux density amplitude in the core is 0.25 T and the winding current amplitude is 42.4 A. The LFECL density distribution in the core under fundamental-frequency current excitation without considering surface ribbons saturation is shown in Fig. 3(a). The LFCL density distribution in the core without considering surface ribbons saturation is shown in Fig. 3(b). While the main flux induced core loss density is about 14 kW/m$^3$ under $B_m$ = 0.25 T, the maximum LFECL density and maximum LFCL density in core surface areas are about 4000 and 350 times of the main flux induced core loss density respectively. Despite the very high LFECL density and LFCL density, the LFECL, LFCL, and main flux induced core loss are 8.2, 0.03, and 5.0 W, respectively.

It should be noted that the surface ribbons of nanocrystalline core HFT may saturate under load condition due to the concentration of leakage flux [27]. The surface ribbons saturation can slightly change the LFECL and LFCL. However, the surface ribbons saturation effect is not considered in the simulation results of Figs. 2 and 3. The reason for not considering surface ribbons saturation is that calculating the practical electromagnetic fields in the core considering surface ribbons saturation requires time-domain FE model with nonlinear *B-H* curve, homogenized FE method, and fine meshes of core surface area. This complex FE model is very time-consuming and of poor convergence. In addition, the FE simulation results in Figs. 2 and 3 are intended to demonstrate the very high LFPL density in core surface areas

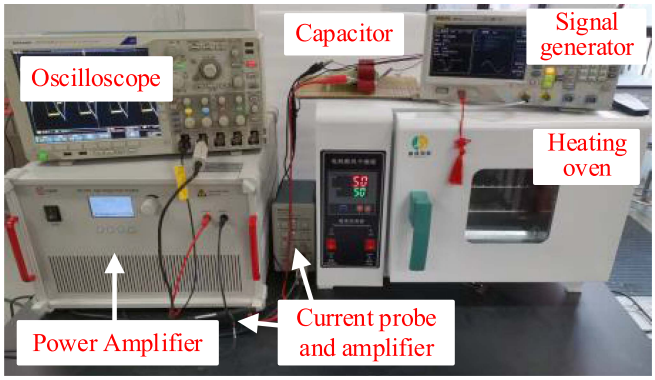


Fig. 4. Core loss test platform for nanocrystalline core.

compared with main flux core loss density and neglecting the surface ribbons saturation will not result in a change in the conclusion.

In our previous paper [27], the significance of LFPL in total power loss of nanocrystalline core HFT is demonstrated and a high-accuracy LFPL calculation method is proposed for the first time. In this section, the LFPL density distribution in the core is further illustrated. These research results demonstrate that the LFPL not only accounts for a high proportion of HFT power loss, but also has high densities in core surface areas. The high LFECL density and LFCL density in core surface areas can result in local temperature hotspot, especially for high-voltage, high-power, and magnetic-integrated HFT. The research results in this section serve as foundations for the subsequent sections of this article, which will present a high-accuracy prediction method and characteristics of thermal field in nanocrystalline core HFT.

## III. Thermal Field Prediction Method Considering LFPL

### A. Temperature Dependence Analysis of HFT Power Losses

Temperature can change the permeability and conductivity of nanocrystalline ribbons as well as the conductivity of copper. Therefore, the main flux induced core loss, LFPL, and winding loss are all temperature-dependent. The temperature dependences of power losses will impact the HFT temperatures and will be analyzed in this section.

*1) Temperature Dependence of Main Flux Induced Core Loss:* A core loss test platform as shown in Fig. 4 is built to measure the nanocrystalline core losses under different temperatures. The toroidal nanocrystalline core under test is placed inside the heating oven to adjust the core temperature. The two-winding method is used to measure the core loss. The primary winding is excited by a power amplifier and the secondary winding is open-circuited. The secondary voltage and primary current waveforms are measured by an oscilloscope and used to calculate the core loss.

The measured nanocrystalline core losses under different temperatures are shown in Fig. 5. The nanocrystalline core loss

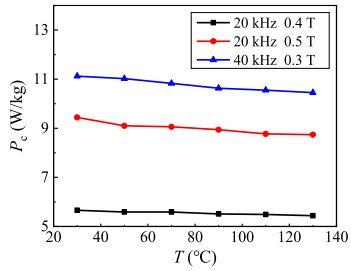


Fig. 5. Measured nanocrystalline core losses under different temperatures.

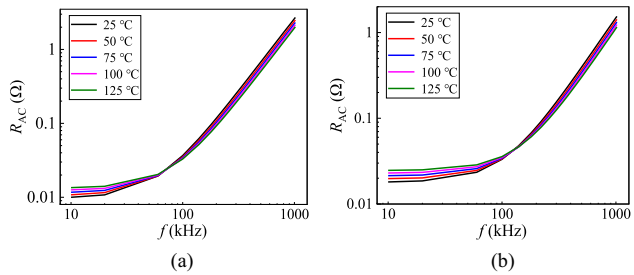


Fig. 6. Variations of winding AC resistance with frequency under different temperatures for (a) the first HFT prototype and (b) the second HFT prototype.

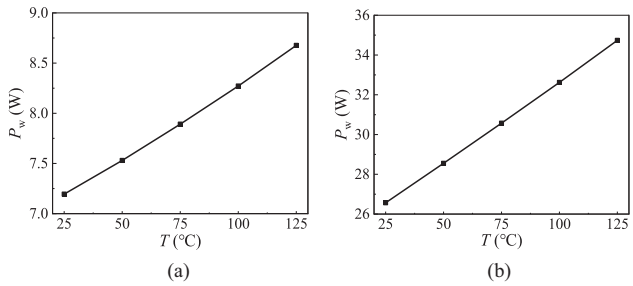


Fig. 7. Variations of winding loss with temperature for (a) the first HFT prototype under load condition ($B_m = 0.32$T, $\varphi = 25°$, natural cooling) and (b) the second HFT prototype under load condition ($B_m = 0.25$T, $\varphi = 25°$, natural cooling).

decreases with the increase of temperature. When the temperature increases from 30 °C to 130 °C, the variation of core loss is within 8% .

*2) Temperature Dependence of Winding Loss:* The conductivity of copper decreases with the increase of temperature. With the decrease of copper conductivity, the dc resistance of copper wire increases while the ac resistance of copper wire decreases. Taking the two nanocrystalline core HFT prototypes as examples, the variations of winding ac resistances with frequency under different temperatures are shown in Fig. 6(a) and (b). At low frequencies, the dc resistance dominates the total ac resistance, so the ac resistance increases with the increase of temperature. At higher frequencies, the skin depth increases with the increase of temperature. The skin effect and proximity effect dominate the total ac resistance, so the ac resistance decreases with the increase of temperature at higher frequencies.

The variations of winding loss with temperature for the two HFT prototypes are shown in Fig. 7(a) and (b). They show that the winding loss increases with the increase of temperature. For the first HFT prototype, when the temperature increases

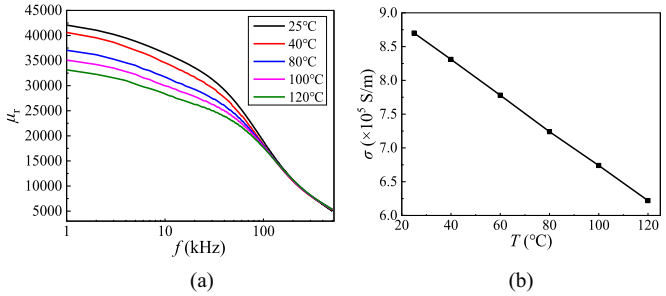


Fig. 8. Variations of (a) permeability with frequency under different temperatures and (b) conductivity with temperature for nanocrystalline ribbon.

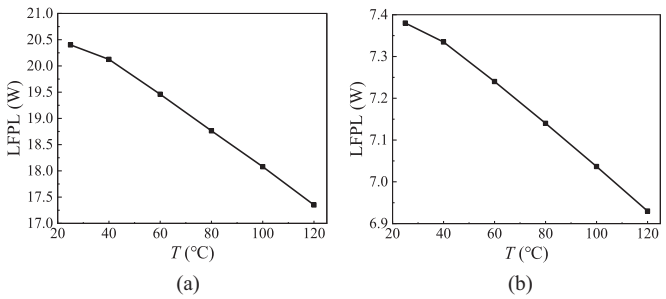


Fig. 9. Variations of LFPL with temperature caused by varied permeability and conductivity for (a) the first HFT prototype under load condition ($B_m = 0.32$T, $\varphi = 25°$, natural cooling) and (b) the second HFT prototype under load condition ($B_m = 0.25$T, $\varphi = 25°$, natural cooling).

from 25 °C to 75 °C and from 25 to 125 °C, the winding loss increases by 9.7% and 20.7% respectively. For the second HFT prototype, when the temperature increases from 25 °C to 75 °C and from 25 to 125 °C, the winding loss increases by 15.1% and 30.8% respectively. Since temperature significantly changes the winding loss, the temperature dependence of winding loss should be considered in thermal field prediction.

*3) Temperature Dependence of LFPL:* Temperature changes the permeability and conductivity of nanocrystalline ribbons, thus changing the leakage flux density and leakage flux eddy current density distributions in the core and varying the LFPL. The variation of permeability with frequency under different temperatures is shown in Fig. 8(a). It shows that the permeability decreases with the increase in frequency. At low frequency (<100 kHz), the permeability decreases with the increase of temperature. At higher frequency (>100 kHz), the variation of permeability with temperature is small. The variation of conductivity of nanocrystalline ribbon with temperature is shown in Fig. 8(b). It shows that the ribbon conductivity decreases with the increase of temperature. When the temperature increases from 25 °C to 120 °C, the conductivity decreases by about 30% .

The variations of LFPL with temperature caused by varied permeability and conductivity for the two HFT prototypes are shown in Fig. 9(a) and (b). It shows that the LFPL decreases with the increase of temperature. When the temperature increases from 25 °C to 120 °C, the LFPL decreases by 15.0% and 6.1% respectively for the two HFT prototypes. Therefore, the temperature dependence of LFPL should be considered in thermal field prediction.

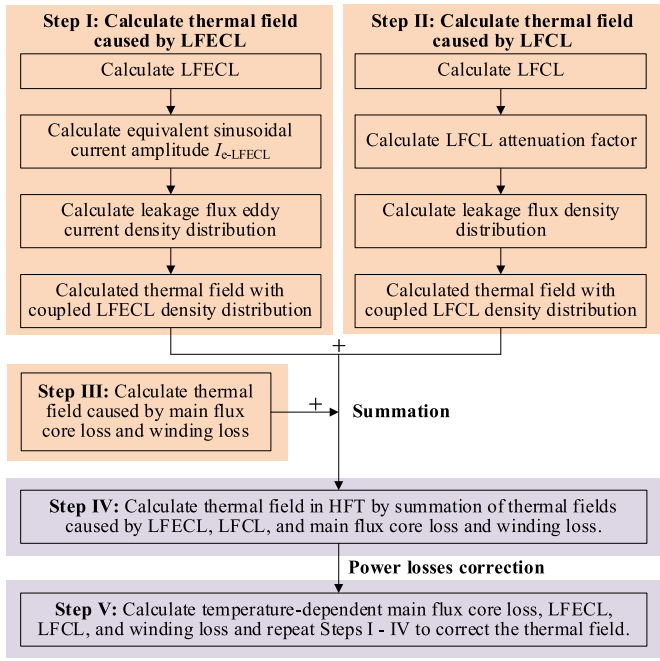


Fig. 10. Flowchart of the proposed thermal field prediction method.

## B. Principle of the Proposed Method

The LFECL density and LFCL density distributions in nanocrystalline core are very nonuniform, which are determined by core structure and sizes, winding structure and sizes, and excitation conditions. It is difficult to predict the LFECL and LFCL loss density distributions and assign these power losses to the corresponding elements of magnetic core in thermal field calculation. In this article, a coupled thermal field prediction method for nanocrystalline core HFT considering LFPL is proposed. The temperature dependences of LFECL, LFCL, main flux core loss, and winding loss are taken into consideration for high-accuracy thermal field prediction.

The flowchart of the proposed method is shown in Fig. 10. The thermal field of nanocrystalline core HFT can be calculated by the summation of thermal fields caused by LFECL, LFCL, and main flux induced core loss and winding loss. A unidirectional magnetic-thermal coupled method is adopted to calculate the thermal fields in HFT caused by LFECL and LFCL. The LFECL density and LFCL density distributions in the core are calculated by magnetic field module with equivalent frequency domain simulation in FE software and then coupled to the heat transfer module to calculate thermal fields. The thermal field caused by main flux core loss and winding loss is calculated by the heat transfer module with uniform power loss densities. Two rounds of calculations are conducted to calculate the thermal field incorporating temperature effects. In the first round of calculation, the temperature dependences of power losses are neglected and the power losses under room temperature are adopted. After the initial calculation, the power losses are corrected with real temperatures and the thermal field is recalculated with the temperature-dependent power losses to achieve high precision. The details of the principle of the proposed thermal field prediction method are described as follows.

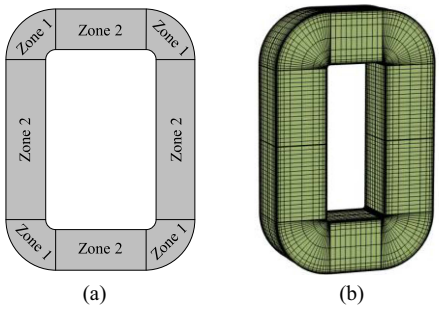


Fig. 11. (a) Zone-divided model. (b) Mesh of the homogenized nanocrystalline core.

**Three other thermal field prediction methods for comparisons**

| |
|---|
| **Method I**<br>Thermal field prediction assuming LFPL uniformly distributed in thin layers on the surface of the core. |
| **Method II**<br>Thermal field prediction assuming LFPL uniformly distributed in the core. |
| **Method III**<br>Thermal field prediction without considering LFPL. |

Fig. 12. Three other thermal field prediction methods for comparisons.

A FE model of nanocrystalline core HFT should be established for electromagnetic field and thermal field calculations. The homogenization method [25] is used for modelling of the nanocrystalline core. The anisotropic conductivity and permeability parameters are used to characterize the homogenized core. A zone-divided approach, as shown in Fig. 11(a), is used for meshing of the core. Zone 1 is modeled in the cylindrical coordinate system and Zone 2 is modeled in the Cartesian coordinate system. Mapping and sweeping methods are applied to generate a mesh in the core region. In addition, to accurately calculate the flux density and eddy current density distributions in surface ribbons of the core, the mesh of core surface is refined. The thickness of surface mesh should be smaller than the thickness of the surface flux density and eddy current density layers. The complete mesh of the nanocrystalline core is shown in Fig. 11(b). The windings are modelled as homogenized multiturn conductors to simplify the computation. The free tetrahedral mesh is used to mesh the windings, epoxy resin, and the remaining air domain.

The first step is prediction of thermal field in HFT caused by LFECL. The LFECL resistances $R_{\mathrm{LFECL}}$ at different harmonic frequencies are calculated by the homogenized FE method proposed in [25]. The air gap and frequency-dependent permeability should be taken into considerations for accurate calculation of $R_{\mathrm{LFECL}}$. The LFECL under nonsinusoidal current excitation is calculated by summation of LFECLs under all harmonic current excitations. Since leakage flux is concentrated in surface ribbons of nanocrystalline core, the surface ribbons may saturate under load condition [26], [27]. The LFECL considering surface ribbons saturation is calculated by the method proposed in [27]. The LFECL calculation equation is shown in the following equation:

$$P_{\mathrm{LFECL}} = k_{\mathrm{LFECL}} \sum_{n=1}^{N} I_n^2 R_{\mathrm{LFECL},n} \tag{1}$$

where $P_{\mathrm{LFECL}}$ is LFECL under load condition considering surface ribbons saturation, $I_n$ is RMS of $n$th-order current, $R_{\mathrm{LFECL},n}$ is LFECL resistance at $n$th-order harmonic frequency, $k_{\mathrm{LFECL}}$ is LFECL multiplication factor considering surface ribbons saturation.

Though the excitation frequency and surface ribbons saturation can change the leakage flux eddy current density distribution in the core, the changes are small and their impacts on thermal field can be neglected. Calculation of LFECL density distribution under nonsinusoidal current excitation considering surface ribbons saturation requires fine meshes, nonlinear *B-H* relationship, and time domain computation. Therefore, calculating the actual LFECL density distribution and then coupling it to the heat transfer module to calculate thermal field are very difficult and time-consuming. In this article, an equivalent sinusoidal current amplitude $I_{e\text{-LFECL}}$ is proposed to make the LFECL under this sinusoidal current excitation without considering surface ribbons saturation the same as the actual LFECL. The $I_{e\text{-LFECL}}$ can be calculated by

$$I_{e-\mathrm{LFECL}} = \sqrt{\frac{2 \times P_{\mathrm{LFECL}}}{R_{\mathrm{LFECL,fund}}}} \tag{2}$$

where $R_{\mathrm{LFECL,fund}}$ is the LFECL resistance under fundamental-frequency sinusoidal current excitation.

After obtaining $I_{e\text{-LFECL}}$, a frequency domain FE simulation under short-circuit excitation is conducted. The secondary winding of HFT is short-circuited and the primary winding is excited with sinusoidal current with an amplitude of $I_{e\text{-LFECL}}$. The calculated leakage flux eddy current density distribution can be assumed similar to the actual distribution, and the calculated LFECL is the same as the actual LFECL. Then, the calculated LFECL density is coupled to the heat transfer module to calculate the thermal field in HFT. The boundary conditions, such as natural convection cooling or forced air cooling, should be set up properly. The anisotropic thermal conductivities of the homogenized nanocrystalline core and surface-to-environment radiation of HFT external surface should be considered. The windings are homogenized and equivalent anisotropic thermal conductivities of the homogenized windings are adopted.

The second step is prediction of thermal field in HFT caused by LFCL. The LFCL is calculated by subtraction of main flux induced core loss from practical flux induced core loss. Both the main flux induced core loss and practical flux induced core loss can be calculated by improved generalized Steinmetz equation (IGSE) [28]. Since the surface ribbons saturation of nanocrystalline core can slightly reduce the LFCL, an LFCL attenuation factor $k_{\mathrm{LFCL}}$ is proposed in [27] to correct the LFCL. The LFCL density considering surface ribbons saturation $P_{\mathrm{LFCL\_sat}}$ can be calculated by

$$P_{\mathrm{LFCL\_sat}}(x,y,z) = k_{\mathrm{LFCL}} \times P_{\mathrm{LFCL\_unsat}}(x,y,z)$$

$$= k_{\mathrm{LFCL}} \times \left[P_{\mathrm{c\_unsat}}(x,y,z,B_{\mathrm{prac}}) - P_{\mathrm{c\_unsat}}(x,y,z,B_{\mathrm{main}})\right] \tag{3}$$

where $P_{\mathrm{LFCL\_unsat}}$ is LFCL without considering surface ribbons saturation, $P_{c\_\mathrm{unsat}}$ is core loss without considering surface ribbons saturation, $B_{\mathrm{prac}}$ and $B_{\mathrm{main}}$ are practical flux density and main flux density at position ($x$,$y$,$z$).

The LFECL multiplication factor $k_{\mathrm{LFECL}}$ and LFCL attenuation factor $k_{\mathrm{LFCL}}$ can be calculated by the method proposed in [27]. First, frequency-domain FE model with practical $\mu$-$B$ curve is used to calculate the leakage flux eddy current density and leakage flux density distributions as well as LFECL $P_{\mathrm{le,sat}}$ and LFCL $P_{\mathrm{lc,sat}}$ considering surface ribbons saturation. Then, frequency-domain FE model with constant $\mu$ value is used to calculate the leakage flux eddy current density and leakage flux density distributions as well as LFECL $P_{\mathrm{le,unsat}}$ and LFCL $P_{\mathrm{lc,unsat}}$ without considering surface ribbons saturation. Finally, the $k_{\mathrm{LFECL}}$ can be calculated by the ratio of $P_{\mathrm{le,sat}}$ and $P_{\mathrm{le,unsat}}$, and the $k_{\mathrm{LFCL}}$ can be calculated by the ratio of $P_{\mathrm{lc,sat}}$ and $P_{\mathrm{lc,unsat}}$.

Frequency-domain FE simulation under short-circuit excitation is conducted to calculate the leakage flux density distribution in the core. The secondary winding of HFT is short-circuited and the primary winding is excited with sinusoidal excitation. The equation (3) is used to calculate the LFCL density distribution. Then, the calculated LFCL density is coupled to the heat transfer module to calculate the thermal field in HFT. The setups of boundary condition and thermal parameters in this step are the same as the setups in the first step. It should be noted that the LFCL density cannot be calculated directly in the magnetic field module in FE software. Therefore, the LFCL density expression in magnetic field module should be modified using (3).

The third step is prediction of thermal field in HFT caused by main flux induced core loss and winding loss. The main flux induced core loss $P_c$ is estimated by the IGSE [28]

$$P_c = \frac{1}{T}\int_0^T k_i \left|\frac{\mathrm{d}B(t)}{\mathrm{d}t}\right|^{\alpha} (\Delta B)^{\beta-\alpha}\mathrm{d}t \tag{4}$$

where $k$, $\alpha$, and $\beta$ are Steinmetz coefficients, $T$ is the period, $B(t)$ is the flux density waveform, and $\triangle B$ is the peak-to-peak value of $B(t)$

$$k_i = \frac{k}{2^{\beta+1}\pi^{\alpha-1}(0.2761 + \frac{1.7061}{\alpha+1.354})}. \tag{5}$$

The winding loss $P_w$ is calculated by summation of winding losses under all harmonic current excitation

$$P_w = \sum_{n=1}^{N} I_n^2 R_{\mathrm{AC},n} \tag{6}$$

where $I_n$ is rms of the $n$th-order harmonic current, $R_{\mathrm{AC},n}$ is the winding ac resistance at the $n$th-order harmonic frequency. The winding ac resistance $R_{\mathrm{AC},n}$ is calculated by summation of skin effect resistance and proximity effect resistance with the method proposed in [29] as shown in (7). The skin effect resistance is calculated by the first term in (7). The proximity effect resistance is calculated by the second term in (7) with macroscopic complex permeability, with which the litz wire can be modelled with homogenized model and calculated through magnetostatic field analysis

$$R_{\mathrm{AC}} = F_{\mathrm{skin}} R_{\mathrm{DC}} + \int_{\Omega_c} \frac{j\omega\dot{\mu}|H|^2}{I^2}\mathrm{d}V \tag{7}$$

$$F_{\mathrm{skin}} = \frac{d_s}{2\sqrt{2}\delta}\frac{\mathrm{ber}(\gamma)\mathrm{bei}'(\gamma) - \mathrm{bei}(\gamma)\mathrm{ber}'(\gamma)}{\mathrm{ber}'^2(\gamma) + \mathrm{bei}'^2(\gamma)} \tag{8}$$

$$R_{\mathrm{DC}} = \frac{l}{N_s \pi {r_s}^2 \sigma} \tag{9}$$

$$\langle\dot{\mu}\rangle = \mu_0\left(1 + \frac{2\eta(\dot{\mu}_r - 1)}{2 + (1-\eta)(\dot{\mu}_r - 1)}\right) \tag{10}$$

$$\dot{\mu}_r = \mu_r \frac{J_1(z)}{zJ_0(z) - J_1(z)} \tag{11}$$

where $F_{\mathrm{skin}}$ is the skin effect coefficient, $R_{\mathrm{DC}}$ is winding dc resistance, $\omega$ is the angular frequency, $f$ is the frequency, $I$ is the winding current, $\delta = \sqrt{1/(\pi f \mu_0 \sigma)}$, $\gamma = d_s/\sqrt{2}\delta$, $d_s$ is the diameter of strand, $r_s$ is the radius of strand, $N_s$ is the number of strand, $l$ is the length of a litz wire, $\sigma$ is the conductivity of copper, $\eta$ is the filling factor, ber($\cdot$) and bei($\cdot$) are real part and imaginary part of Bessel function, respectively, $J_n$ is the $n$th-order Bessel function, $\mu_r$ is the relative permeability, and $H$ is the magnetic field in winding area. The magnetic field $H$ can be calculated by analytical model or FE model with image method.

After calculating the main flux induced core loss and winding loss, they are uniformly distributed to the core and windings. The heat transfer module in FE software is used to calculate the thermal field caused by main flux induced core loss and winding loss. The setups of boundary condition and thermal parameters in this step are the same as the setups in the first step.

The fourth step is summation of thermal fields caused by LFECL, LFCL, and main flux induced core loss and winding loss to obtain a preliminary prediction result of thermal field in nanocrystalline core HFT. The temperatures of core and windings can be extracted from the preliminary prediction result for further high-accuracy power loss estimations.

The final step is recalculating the thermal field through Steps I–IV with temperature-dependent LFECL, LFCL, core loss, and winding loss to achieve high-accuracy thermal field prediction. The permeability and conductivity of nanocrystalline ribbons, main flux core loss, and copper conductivity are corrected with the preliminary calculated temperatures for high-accuracy power losses and thermal field estimation. Though the preliminary calculated temperatures may differ from the practical temperatures, the deviations are very small and the resulting errors can be neglected.

### C. Methods for Comparison

Three other thermal field prediction methods as shown in Fig. 12 are implemented for comparisons to illustrate the necessity and accuracy of the proposed method.

The first comparison method is separating thin layers on the surface of nanocrystalline core and assuming the LFECL and LFCL to be uniformly distributed in the surface thin layers. The concentration of LFPL on core surface areas is considered

in this method. However, the precise nonuniform distribution characteristic of LFPL is not considered. The LFPL density in leakage flux concentration region may be underestimated and the hotspot temperature in HFT may be underestimated.

The second comparison method is based on the assumption that the LFPL are uniformly distributed in the core. Therefore, the total core loss is calculated by summation of main flux induced core loss, LFECL, and LFCL and then uniformly distributed to the core. The value of LFPL is taken into account in this method. However, the nonuniform distribution of LFPL is completely not considered and the hotspot temperature of HFT may be also underestimated.

The third comparison method is thermal field prediction without considering LFPL, with only main flux induced core loss and winding loss considered. Since the LFPL has not received enough attention before, this method is commonly adopted in the optimization and thermal field prediction of nanocrystalline core HFT.

The significance of LFPL in core loss of nanocrystalline core HFT is demonstrated for the first time in our previous article [27]. In addition, a high-accuracy LFPL calculation method is proposed in [27] for the first time. At present, a precise thermal field prediction method for nanocrystalline core HFT considering the LFPL is lacking. The third comparison method is a common industry practice in thermal field prediction, with consideration of only main flux core loss and winding loss. The first two comparison methods are two simple methods, which can consider the LFPL, but cannot consider the precise LFPL distribution. The third comparison method is used to demonstrate the need of considering the LFPL component, while the first two comparison methods are used to demonstrate the necessity of considering the precise LFPL distribution in core surface areas.

The frequency domain superposition method, in which the thermal field caused by LFPL is calculated by the summation of thermal fields under all harmonic excitations, is time-consuming since the thermal field under each harmonic excitation should be calculated with the magnetic-thermal coupled method separately. In addition, the Fourier decomposition method will fail when surface ribbons of nanocrystalline core saturate and the core shows a nonlinear characteristic. Therefore, the frequency domain superposition method can lead to both long computation time and low calculation accuracy and is thus not compared in this article.

## IV. Experimental Verification and Thermal Field Analysis

### A. Experimental Platform

Two nanocrystalline core HFT prototypes are made to validate the proposed thermal field prediction method and investigate the thermal field characteristics. The structures and dimensions of the two HFT prototypes are shown in Fig. 1. The HFTs are fully potted by epoxy resin with high thermal conductivity. The pictures of the two HFT prototypes are shown in Fig. 13. To measure the HFT temperature, several K-type thermocouples are buried inside the HFTs before potting. The temperature measurement

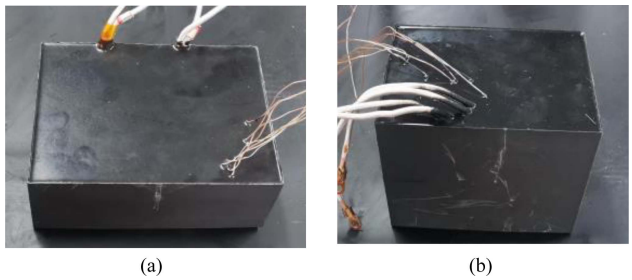


Fig. 13. Pictures of two HFT prototypes. (a) Rectangular core with separated windings. (b) EE core with concentric windings.

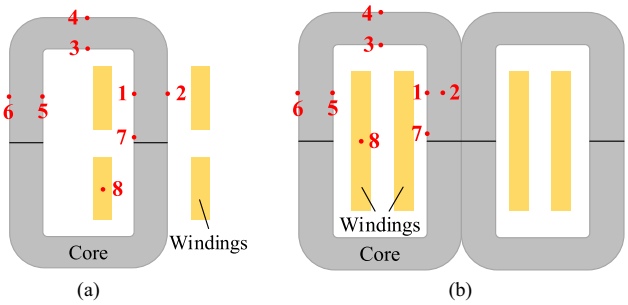


Fig. 14. Positions of K-type thermocouples inside the two HFT prototypes. (a) First HFT prototype. (b) Second HFT prototype.

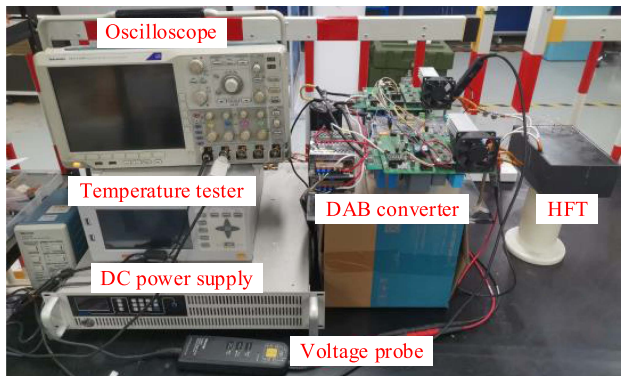


Fig. 15. HFT temperature test platform.

error of the K-type thermocouple is within ±1.5 °C. The positions of the K-type thermocouples are shown in Fig. 14. The spatial position errors of the attached thermocouples are within ±0.5 mm.

An HFT temperature test platform is established as shown in Fig. 15. A DAB converter is used to provide load excitations to the HFT prototypes. A dc power supply is used to provide dc power to the DAB converter. The temperatures of HFT prototypes under natural cooling condition are measured by K-type thermocouples with a multichannel temperature tester. When the HFT prototypes work under thermal equilibrium states, the steady-state temperatures of HFTs will be recorded.

### B. Validation of the Proposed Method

The temperature calculation results and errors of the first HFT prototype at different flux density amplitudes $B_m$, phase

shift angles $\varphi$, and natural cooling condition are shown in Fig. 16(a)–(c). With the comparison method III, the temperatures of the HFT prototype will be greatly underestimated. The hotspot temperature can be underestimated by 30–60 °C. The comparison method I and method II will slightly overestimate the temperatures at positions 3, 4, 5, and 6 while greatly underestimate the temperatures at positions 1, 2, 7, and 8. The hotspot temperature underestimations can be over 20 °C. The reasons for the temperature estimation errors are that the power loss densities at positions 3, 4, 5, and 6 are overestimated and the power loss densities at positions 1, 2, and 7 are underestimated. With the proposed method, the temperature prediction errors are below 3 °C and most of the errors are below 2 °C.

The temperature calculation results and errors of the second HFT prototype at different flux density amplitudes $B_m$, phase shift angles $\varphi$, and natural cooling condition are shown in Fig. 17(a)–(c). With the comparison method III, the hotspot temperatures of the HFT prototype can be underestimated by over 15 °C. Though the temperature prediction accuracy can be improved with the comparison methods I and II, the hotspot temperatures can still be underestimated by 5–10 °C. With the proposed method, the HFT temperature prediction errors will be reduced to below 3 °C and most of the errors are below 1.5 °C.

The surface temperatures of the two HFT prototypes are measured by an infrared camera and compared with the calculation results to further validate the proposed method. When the first HFT prototype works under load condition ($B_m$ = 0.32T, $\varphi$ = 25°, natural cooling), the calculated and measured surface temperatures are shown in Fig. 18. The deviations between the calculated and measured surface temperatures are below 2 °C. When the second HFT prototype works under load condition ($B_m$ = 0.25T, $\varphi$ = 25°, natural cooling), the calculated and measured surface temperatures are shown in Fig. 19. The deviations between the calculated and measured surface temperatures are below 4 °C. The measurement error of the infrared camera is within ±2 °C. In addition, the surface emissivity of epoxy resin and environment conditions will also affect the measurement results. Therefore, the temperature prediction accuracy as demonstrated in Figs. 18 and 19 with the proposed method is satisfactory.

The impacts of temperature dependences of power losses on HFT temperatures are analyzed with the proposed method. The thermal field calculation results and deviations for the first HFT prototype with temperature-independent power losses under load condition ($B_m$ = 0.32T, $\varphi$ = 25°, natural cooling) are shown in Fig. 20. With temperature-independent core loss, the temperatures are overestimated and the temperature calculation deviations are below 1 °C. With temperature-independent winding loss, the temperatures are underestimated and the temperature calculation deviations are below 2 °C. Therefore, the impacts of temperature dependences of core loss and winding loss on HFT temperatures are weak. However, with temperature-independent LFPL, the temperatures are overestimated and the maximum temperature calculation deviation exceeds 6 °C. Therefore, the impact of temperature dependence of LFPL on HFT temperatures are significant and should not be neglected.

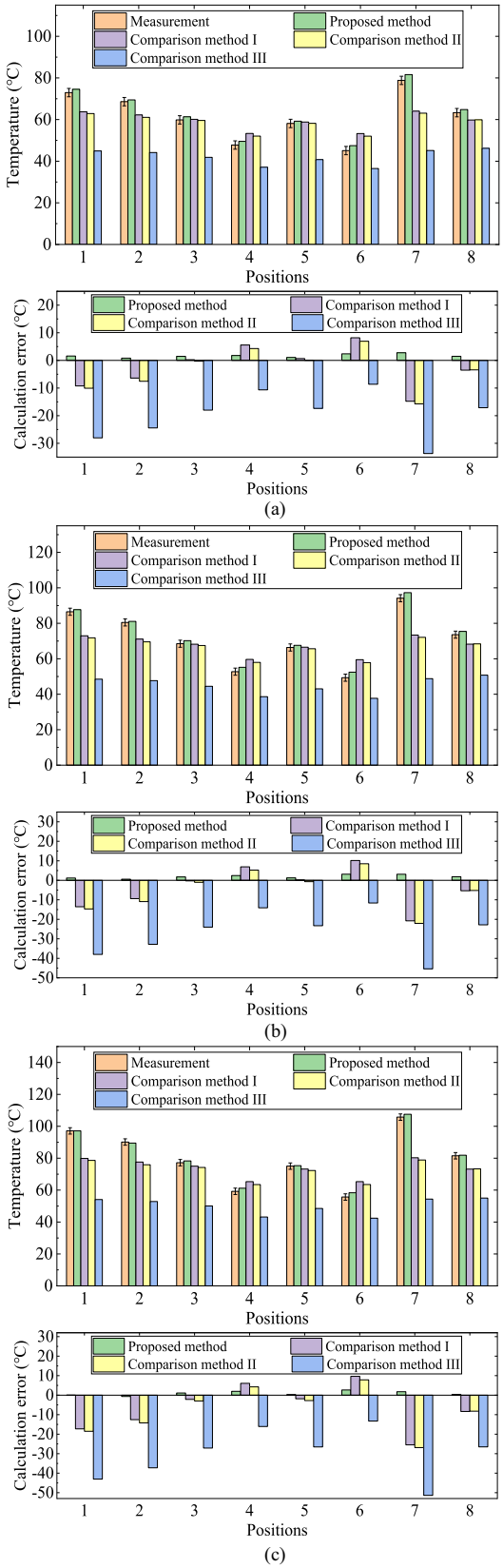


Fig. 16. Temperature calculation results and errors of the first HFT prototype with rectangular core and separated windings. (a) $B_m$ = 0.24T, $\varphi$ = 30°, natural cooling. (b) $B_m$ = 0.24T, $\varphi$ = 35°, natural cooling. (c) $B_m$ = 0.32T, $\varphi$ = 25°, natural cooling.

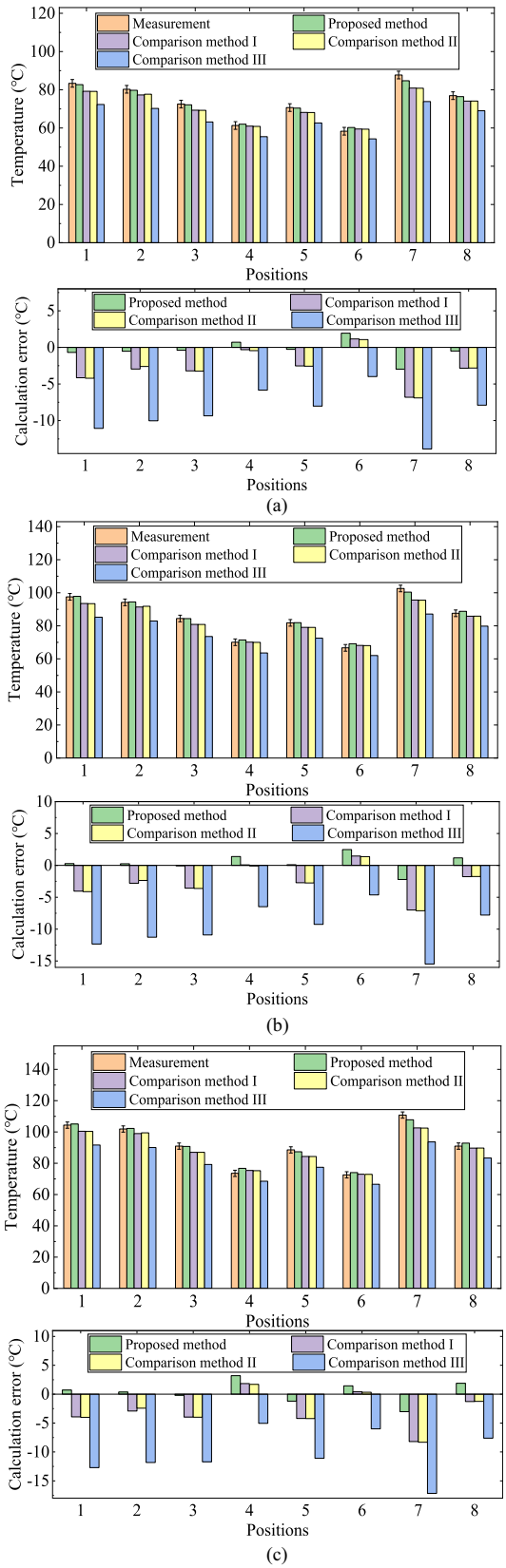


Fig. 17. Temperature calculation results and errors of the second HFT prototype with dual-rectangular core and concentric windings. (a) $B_m = 0.14$T, $\varphi = 45°$, natural cooling. (b) $B_m = 0.18$T, $\varphi = 35°$, natural cooling. (c) $B_m = 0.25$T, $\varphi = 25°$, natural cooling.

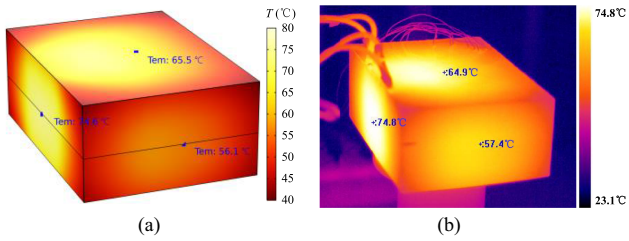


Fig. 18. (a) Calculated and (b) measured surface temperatures of the first HFT prototypes under load condition ($B_m = 0.32$T, $\varphi = 25°$, natural cooling).

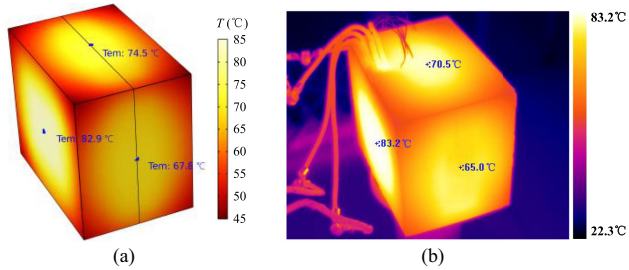


Fig. 19. (a) Calculated and (b) measured surface temperatures of the second HFT prototypes under load condition ($B_m = 0.25$T, $\varphi = 25°$, natural cooling).

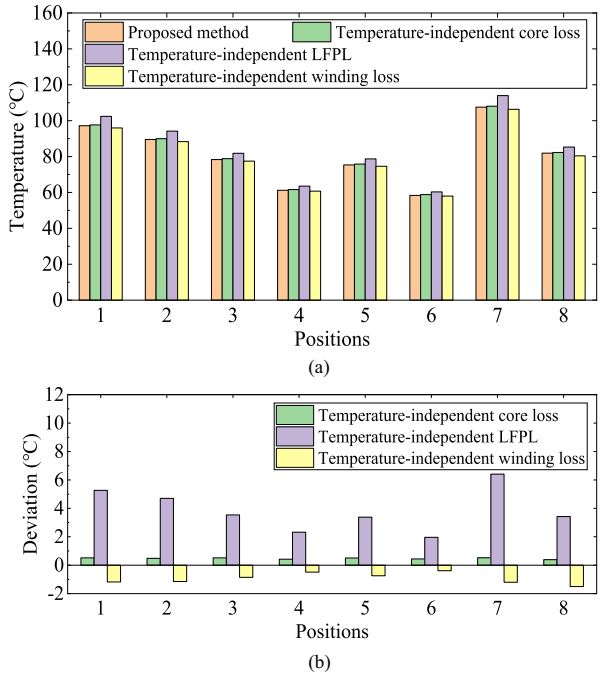


Fig. 20. Thermal field calculation (a) results and (b) deviations for the first HFT prototype under load condition ($B_m = 0.32$T, $\varphi = 25°$, natural cooling).

The thermal field calculation results and deviations for the second HFT prototype with temperature-independent power losses under load condition ($B_m = 0.25$T, $\varphi = 25°$, natural cooling) are shown in Fig. 21. With temperature-independent core loss, the temperatures are overestimated and the temperature calculation deviations are below 1 °C. With temperature-independent LFPL, the temperatures are overestimated and the temperature calculation deviations ar also below 1 °C. Therefore,

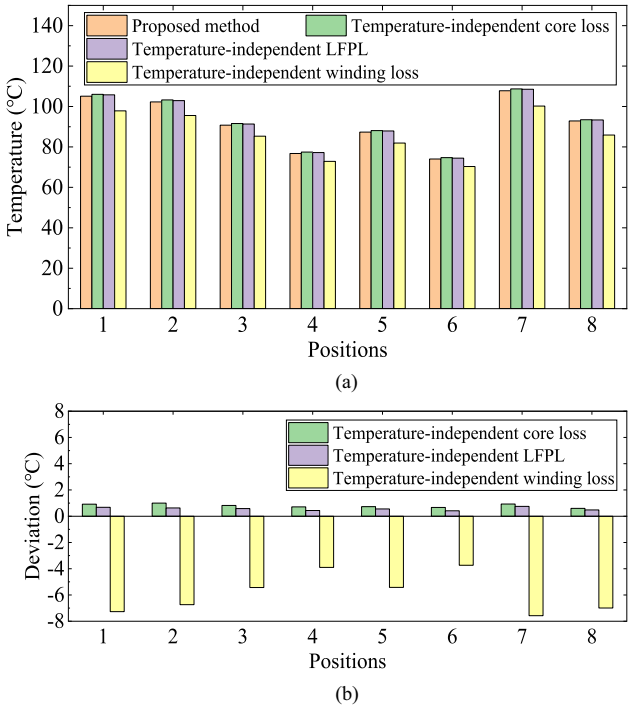


Fig. 21. Thermal field calculation (a) results and (b) deviations for the second HFT prototype under load condition ($B_m = 0.25$T, $\varphi = 25°$, natural cooling).

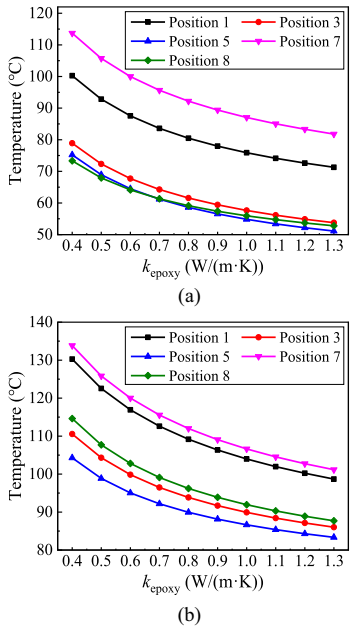


Fig. 22. Variations of HFT temperatures with thermal conductivity of epoxy resin $k_{\text{epoxy}}$ for (a) the first HFT prototype under load condition ($B_m = 0.32$T, $\varphi = 25°$, natural cooling) and (b) the second HFT prototype under load condition ($B_m = 0.25$T, $\varphi = 25°$, natural cooling).

the impacts of temperature dependences of core loss and LFPL on HFT temperatures are weak. However, with temperature-independent winding loss, the HFT temperatures are underestimated and the maximum temperature calculation deviation exceeds 7 °C. Therefore, the impact of temperature dependence of winding loss on HFT temperatures are significant and should not be neglected.

The thermal conductivity of epoxy resin can change the thermal field of HFT. The thermal conductivity of epoxy resin used in these two HFT prototypes is about 0.9 W/(m·K). The variations of HFT temperatures with thermal conductivity of epoxy resin are calculated with the proposed method and shown in Fig. 22. It shows that the HFT temperatures decrease with the increase of $k_{\text{epoxy}}$. When the $k_{\text{epoxy}}$ increases from 0.4 to 1.3 W/(m·K), the HFT temperatures drop by 15–30 °C and 20–35 °C, respectively, for the two HFT prototypes. In addition, with the increase of $k_{\text{epoxy}}$, the HFT temperature decreasing rate decreases. Furthermore, when the $k_{\text{epoxy}}$ increases from 0.8 to 0.9 W/(m·K) and from 0.9 to 1.0 W/(m·K), the temperature variations are within 2.5 and 3 °C, respectively, for the two HFT prototypes. Therefore, a small deviation in $k_{\text{epoxy}}$ will not result in large prediction errors in thermal field of HFT.

The spatial coordinates of temperature calculation points in the FE models are changed in the range of ±0.5 mm to compare the temperature deviations and investigate the temperature measurement errors caused by thermocouple position errors. For the first HFT prototype, the temperature measurement errors caused by the spatial position errors of thermocouples are within ±0.5 °C. For the second HFT prototype, the temperature measurement errors caused by the spatial position errors of thermocouples are within ±0.2 °C. Since the temperature measurement error of thermocouple is within ±1.5 °C, the temperature measurement error caused by both thermocouple measurement error and spatial position error is within ±2 °C.

In summary, the thermal field prediction errors with the proposed method are acceptable. The thermal field prediction errors may come from several aspects. First, it may come from the simplification of the FE model. Since the practical leakage flux and leakage flux eddy current distributions in the core considering surface ribbons saturation are difficult to calculate, equivalent frequency domain simulations are implemented to calculate them. The deviations between the calculated and actual leakage flux and leakage flux eddy current distributions may result in small temperature prediction errors. Second, the errors may come from the thermal conductivity of epoxy resin in the FE model. A recommended thermal conductivity value is used in the FE model, which may have slight deviations from the actual value. Third, as discussed above, the thermal field prediction errors may come from the spatial position error and measurement error of thermocouples.

### C. Thermal Field Analysis

Adopting the proposed thermal field prediction method, the thermal fields of the two HFT prototypes are analyzed with FE method.

Taking the DAB converter with SPS modulation as an example of load condition, when the first HFT prototype works under load condition ($B_m = 0.32$T, $\varphi = 25°$, natural cooling), the thermal field calculated by FE method with only main flux core loss and winding loss is shown in Fig. 23(a). It shows that the temperature hotspot of HFT is located at core limb, which is surrounded by the windings, whose temperature reaches as high as 55 °C. The thermal field calculated by FE method with only LFECL and LFCL is shown in Fig. 23(b). The temperature distribution in

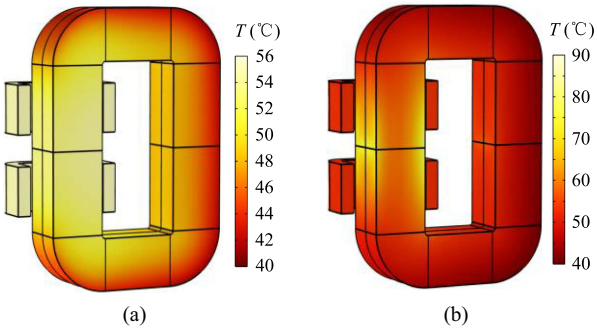


Fig. 23. Thermal field simulation results of the first HFT prototype with (a) only main flux core loss and winding loss and (b) only LFECL and LFCL.

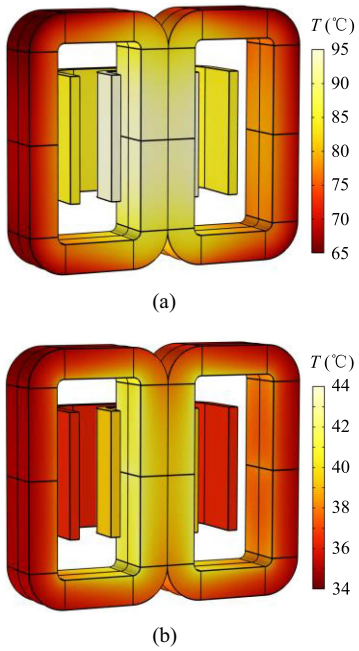


Fig. 24. Thermal field simulation results of the second HFT prototype with (a) only main flux core loss and winding loss and (b) only LFECL and LFCL.

the core limb surrounded by the windings is very nonuniform. The temperature hotspot is located at surface ribbons near the air gap of the core limb surrounded by the windings, reaching as high as 90 °C. This high hotspot temperature is caused by the concentration of LFPL in core surface areas. However, the temperatures of internal ribbons and windings remain low. Therefore, the practical temperature hotspot of HFT under load condition will be located at the surface ribbons near the air gap. The hotspot temperature of HFT will be greatly underestimated without considering the LFPL.

When the second HFT prototype works under load condition ($B_m = 0.25$T, $\varphi = 25°$, and natural cooling), the thermal field calculated by FE method with only main flux core loss and winding loss is shown in Fig. 24(a). It shows that the temperature hotspot of HFT is located at core middle limb, whose temperature reaches as high as 95 °C. The thermal field calculated by the FE method with only LFECL and LFCL is shown in Fig. 24(b). Due to the concentration of LFPL in surface ribbons of core middle limb and high thermal resistance between the surface ribbons and environment, the temperature hotspot is also located at core middle limb, whose temperature reaches as high as 42 °C. Therefore, the practical temperature hotspot of HFT under load condition will be located at core middle limb. The hotspot temperature of HFT will be greatly underestimated without considering the LFPL.

TABLE I
HOTSPOT TEMPERATURE RISES OF THE FIRST HFT PROTOTYPE

| | $\triangle T_m$ (°C) | $\triangle T_l$ (°C) | $\triangle T_t$ (°C) |
|---|---|---|---|
| $B_m = 0.24$T, $\varphi = 30°$, natural cooling | 21.3 | 44.8 | 64.0 |
| $B_m = 0.24$T, $\varphi = 35°$, natural cooling | 25.8 | 59.4 | 82.2 |
| $B_m = 0.32$T, $\varphi = 25°$, natural cooling | 29.1 | 63.9 | 92.3 |

$\triangle T_m$: Temperature rise with only main flux core loss and winding loss.
$\triangle T_l$: Temperature rise with only LFECL and LFCL.
$\triangle T_t$: Temperature rise with total power loss of HFT.

TABLE II
HOTSPOT TEMPERATURE RISES OF THE SECOND HFT PROTOTYPE

| | $\triangle T_m$ (°C) | $\triangle T_l$ (°C) | $\triangle T_t$ (°C) |
|---|---|---|---|
| $B_m = 0.14$T, $\varphi = 45°$, natural cooling | 47.6 | 11.6 | 57.0 |
| $B_m = 0.18$T, $\varphi = 35°$, natural cooling | 61.3 | 14.2 | 73.1 |
| $B_m = 0.25$T, $\varphi = 25°$, natural cooling | 67.5 | 15.1 | 81.3 |

$\triangle T_m$: Temperature rise with only main flux core loss and winding loss.
$\triangle T_l$: Temperature rise with only LFECL and LFCL.
$\triangle T_t$: Temperature rise with total power loss of HFT.

The hotspot temperature rises of the two HFT prototypes are further investigated. As shown in Table I, for the first HFT prototype, the hotspot temperature rises with only main flux core loss and winding loss $\triangle T_m$ are between 20 and 30 °C, while the hotspot temperature rises with only LFECL and LFCL $\triangle T_l$ can reach over twice that of $\triangle T_m$. As shown in Table II, for the second HFT prototype, the hotspot temperature rises with only main flux core loss and winding loss $\triangle T_m$ are between 40 and 70 °C, while the hotspot temperature rises with only LFECL and LFCL $\triangle T_l$ are between 10 °C to 15 °C. It is necessary to take the LFECL and LFCL into considerations in thermal field prediction and design of nanocrystalline core HFT.

Since LFPL significantly increases the hotspot temperature of nanocrystalline core HFT, enhanced cooling strategies may be necessary to avoid high temperature. For example, novel insulation materials with high thermal conductivity such as AlN ceramics or silicone gel can be used for efficient cooling. In addition, heat pipes or water cooling plate can be embedded inside the cast epoxy resin and near the hotspot to remove the internal heat more efficiently. Furthermore, the LFPL suppression methods could be investigated and adopted to reduce the power loss and hotspot temperature.

The proposed thermal field prediction method and characteristics can be extended to HFTs with other magnetic cores with rolling structure, such as amorphous cores. In addition, the development of nanocrystalline core HFT towards high-voltage, high-power, and magnetic-integrated will increase the leakage magnetic field and LFPL. The hotspot temperature of HFT will be greatly underestimated without consideration of LFPL. Therefore, the proposed method is especially helpful and necessary for high-accuracy thermal field prediction of high-voltage, high-power, and magnetic-integrated nanocrystalline core HFT.

## V. Conclusion

This article investigates the LFPL density distribution, proposes a high-accuracy thermal field prediction method with consideration of LFPL, and analyzes the thermal field characteristics for nanocrystalline core HFT. The main conclusions of this article are summarized as follows.

1) The LFPL is concentrated in surface ribbons of nanocrystalline core HFT. The LFPL density in core surface area is very high compared with main flux induced core loss density. The extremely high LFPL density in core surface area can result in additional temperature rise and local increased hotspot temperature.
2) A high-accuracy thermal field prediction method for nanocrystalline core HFT with consideration of LFPL is proposed. The temperature dependences of power losses should be considered for high-accuracy thermal field prediction. The thermal fields caused by the LFPL are calculated by the magnetic-thermal coupled method, in which LFPL densities are calculated by equivalent frequency domain FE simulation and coupled to the heat transfer module to calculate the thermal field. Compared with other methods, the proposed method can reduce the temperature calculation errors from over 20 °C to below 3 °C.
3) The LFPL can increase the hotspot temperature of nanocrystalline core HFT by more than 40 °C and over 10 °C for the two HFT prototypes respectively. Therefore, the LFPL should be taken into consideration for high-accuracy thermal field prediction of nanocrystalline core HFT. Enhanced cooling strategies such as using high-thermal-conductivity insulation materials or embedded heat pipes or water cooling plate may be necessary for efficient cooling of hotspots.

## References


[1] X. She, A. Q. Huang, and R. Burgos, "Review of solid-state transformer technologies and their application in power distribution systems," *IEEE J. Emerg. Sel. Topics Power Electron.*, vol. 1, no. 3, pp. 186–198, Sep. 2013.

[2] X. She, X. Yu, F. Wang, and A. Q. Huang, "Design and demonstration of a 3.6-kV–120-V/10-kVA solid-state transformer for smart grid application," *IEEE Trans. Power Electron.*, vol. 29, no. 8, pp. 3982–3996, Aug. 2014.

[3] T. Liu et al., "Design and implementation of high efficiency control scheme of dual active bridge based 10 kV/1 MW solid state transformer for PV application," *IEEE Trans. Power Electron.*, vol. 34, no. 5, pp. 4223–4238, May 2019.

[4] D. Rothmund, T. Guillod, D. Bortis, and J. W. Kolar, "99% efficient 10 kV SiC-based 7 kV/400 V DC transformer for future data centers," *IEEE J. Emerg. Sel. Topics Power Electron.*, vol. 7, no. 2, pp. 753–767, Jun. 2019.

[5] L. Zheng et al., "Solid-state transformer and hybrid transformer with integrated energy storage in active distribution grids: Technical and economic comparison, dispatch, and control," *IEEE J. Emerg. Sel. Topics Power Electron.*, vol. 10, no. 4, pp. 3771–3787, Aug. 2022.

[6] M. Leibl, G. Ortiz, and J. W. Kolar, "Design and experimental analysis of a medium-frequency transformer for solid-state transformer applications," *IEEE J. Emerg. Sel. Topics Power Electron.*, vol. 5, no. 1, pp. 110–123, Mar. 2017.

[7] M. Mogorovic and D. Dujic, "Sensitivity analysis of medium-frequency transformer designs for solid-state transformers," *IEEE Trans. Power Electron.*, vol. 34, no. 9, pp. 8356–8367, Sep. 2019.

[8] Z. Guo et al., "A novel high insulation 100 kW medium frequency transformer," *IEEE Trans. Power Electron.*, vol. 38, no. 1, pp. 112–117, Jan. 2023.

[9] B. Chen, X. Liang, and N. Wan, "Design methodology for inductor-integrated litz-wired high-power medium-frequency transformer with the nanocrystalline core material for isolated DC-link stage of solid-state transformer," *IEEE Trans. Power Electron.*, vol. 35, no. 11, pp. 11557–11573,

[10] M. Mogorovic and D. Dujic, "100 kW, 10 kHz medium-frequency transformer design optimization and experimental verification," *IEEE Trans. Power Electron.*, vol. 34, no. 2, pp. 1696–1708, Feb. 2019.

[11] Z. Wan, Y. Li, H. Wang, and X. Li, "Optimization design of high-frequency matrix transformer for solid-state transformer," *IEEE Trans. Power Electron.*, vol. 39, no. 10, pp. 12384–12396, Oct. 2024.

[12] M. Jaritz, A. Hillers, and J. Biela, "General analytical model for the thermal resistance of windings made of solid or litz wire," *IEEE Trans. Power Electron.*, vol. 34, no. 1, pp. 668–684, Jan. 2019.

[13] P. A. Kyaw, M. Delhommais, J. Qiu, C. R. Sullivan, J.-L. Schanen, and C. Rigaud, "Thermal modeling of inductor and transformer windings including litz wire," *IEEE Trans. Power Electron.*, vol. 35, no. 1, pp. 867–881, Jan. 2020.

[14] R. Shafaei, M. Ordonez, and M. A. Saket, "Three-dimensional frequency-dependent thermal model for planar transformers in LLC resonant converters," *IEEE Trans. Power Electron.*, vol. 34, no. 5, pp. 4641–4655, May 2019.

[15] F. Chauvicourt, P. Romanazzi, D. Howey, A. Dziechciarz, C. Martis, and C. T. Faria, "Review of multidisciplinary homogenization techniques applied to electric machines," in *Proc. 11th Int. Conf. Ecological Veh. Renewable Energies*, 2016, pp. 1–9.

[16] G. Salinas López, A. D. Expósito, J. Muñoz-Antón, J. Á. O. Ramírez, and R. P. López, "Fast and accurate thermal modeling of magnetic components by FEA-based homogenization," *IEEE Trans. Power Electron.*, vol. 35, no. 2, pp. 1830–1844, Feb. 2020.

[17] P. Li, Q. Li, Y. Zhang, Y. Zhou, L. Zhang, and C. Teng, "Simulation of 500 kHz high frequency transformer temperature rise under different wave excitation," in *Proc. IEEE Int. Conf. High Voltage Eng. Appl.*, 2020, pp. 1–4.

[18] H. Wang et al., "Thermal design consideration of medium voltage high frequency transformers," in *Proc. IEEE Appl. Power Electron. Conf. Expo.*, 2020, pp. 2721–2726.

[19] M. Ngo, Y. Cao, D. Dong, R. Burgos, K. Nguyen, and A. Ismail, "Forced air-cooling thermal design methodology for high-density, high-frequency, and high-power planar transformers in 1U applications," *IEEE J. Emerg. Sel. Topics Power Electron.*, vol. 11, no. 2, pp. 2015–2028, Apr. 2023.

[20] Z. Wang, C. L. Bak, H. Wang, H. Sørensen, and F. F. da Silva, "Multi-physics digital model of the high frequency transformer for power electronics application considering electro-thermal interactions," *IEEE Trans. Power Electron.*, vol. 38, no. 11, pp. 14345–14359, Nov. 2023.

[21] Y. Dang, L. Zhu, F. Liu, F. Zhang, Z. Liu, and S. Ji, "Multilevel boundary-coupled method for the efficient thermal prediction of high-frequency transformers (HFTs) with cylindrical windings," *IEEE Trans. Power Electron.*, vol. 40, no. 4, pp. 5566–5582, Apr. 2025.

[22] Y. Wang, G. Calderon-Lopez, and A. J. Forsyth, "High-frequency gap losses in nanocrystalline cores," *IEEE Trans. Power Electron.*, vol. 32, no. 6, pp. 4683–4690, Jun. 2017.

[23] Y. Wang, G. Calderon-Lopez, and A. Forsyth, "Thermal management of compact nanocrystalline inductors for power dense converters," in *Proc. IEEE Appl. Power Electron. Conf. Expo.*, 2018, pp. 2696–2703.

[24] J. Scoltock, Y. Wang, G. Calderon-Lopez, and A. J. Forsyth, "Rapid thermal analysis of nanocrystalline inductors for converter optimization," *IEEE J. Emerg. Sel. Topics Power Electron.*, vol. 8, no. 3, pp. 2276–2284, Sep. 2020.

[25] Z. Liu, L. Zhu, Y. Dang, C. Zhan, and S. Ji, "Deduction measurement method and high-accuracy calculation model of leakage flux eddy current loss in nanocrystalline core high-frequency transformer," *IEEE Trans. Power Electron.*, vol. 40, no. 4, pp. 5609–5621, Apr. 2025.

[26] Z. Liu, L. Zhu, Y. Dang, and S. Ji, "Efficient calculation method and characterization of practical flux distribution in nanocrystalline core high-frequency transformer under load condition," *IEEE Trans. Power Electron.*, vol. 41, no. 3, pp. 3681–3694, Mar. 2026, doi: 10.1109/TPEL.2025.3610516.

[27] Z. Liu, L. Zhu, Y. Dang, and S. Ji, "Core loss calculation method considering leakage flux induced power loss for nanocrystalline core high-frequency transformer under load condition," *IEEE Trans. Power Electron.*, vol. 40, no. 9, pp. 13126–13141, Sep. 2025.

[28] K. Venkatachalam, C. R. Sullivan, T. Abdallah, and H. Tacca, "Accurate prediction of ferrite core loss with nonsinusoidal waveforms using only Steinmetz parameters," in *Proc. IEEE Workshop Comput. Power Electron.*, 2002, pp. 36–41.

[29] T. Chen, Z. Zhao, Z. Shen, H. Jia, J. Ji, and H. Wang, "Litz-wire winding loss calculation method for optimal design of high-frequency transformers," *IEEE J. Emerg. Sel. Topics Power Electron.*, vol. 12, no. 2,